Chin. J. Astron. Astrophys. Vol. 5 (2005), No. 5, 519–530
(*http://www.chjaa.org*)

Chinese Journal of
Astronomy and
Astrophysics

Multi-wavelength Diagnostics of Bombardment by Non-thermal Particles in Solar Flares *

Zhi Xu[1], Cheng Fang[1] and Wei-Qun Gan[2]

[1] Astronomy Department of Nanjing University, Nanjing 210093; *xuzhi@nju.edu.cn*
[2] Purple Mountain Observatory, Chinese Academy of Sciences, Nanjing 210008

Received 2005 March 24; accepted 2005 May 11

Abstract Chromospheric lines, including Hα, Lyα, Lyβ and CaII K, CaII 8542, are systemically and quantitatively investigated with respect to the non-thermal excitation and ionization due to particle beam bombardment for a series of solar semi-empirical atmospheric models. As a result we propose to use the contrast in the integrated intensity of hydrogen lines to estimate the total energy flux of the bombarding beam during the solar flare impulsive phase. Partial frequency redistribution is considered in the Lyα line calculation and a smaller intensity enhancement in the Hα line-centers is found than in the previous results of Fang et al.

Key words: Sun: flare — Sun: chromosphere

1 INTRODUCTION

Bombardment by non-thermal particle beams is believed to be one of the processes that transfer energy from the place of magnetic reconnection to the solar chromosphere, particularly during the impulsive phase of solar flares. So it is of importance to determine both the fluxes and energy distribution of these particles when attempting to further our understanding of the flare energy release process (Miller et al. 1997). However, particles in solar flares could be accelerated over a wide energy range from keV up to GeV (Voget & Hénoux 1996). Many high energy observations have indicated the existence of non-thermal particles in solar flares: protons of energy of more than 1 MeV can be detected by their γ-ray emission, while non-thermal electrons of deca keV energies can be diagnosed by their hard X-ray and radio emission, and impact linear polarization of chromospheric lines during solar flares, especially without hard X-ray association, can supply complementary evidence for hecto keV protons (Voget & Hénoux 1999; Emslie & Miller 2000).

Intensity profiles can also provide information on the non-thermal particle beams. Although the value of the ratio between the thermal and non-thermal components is still controversial, we know that the semi-empirical atmospheric models of solar flares derived from theoretic considerations that exclude non-thermal ionization and excitation of hydrogen atoms will overestimate

* Supported by the National Natural Science Foundation of China.

the temperature (Fang et al. 1993). Hudson (1972) and Lin & Hudson (1976) first pointed out the significance of non-thermal ionization of hydrogen atoms by electron beams. Emslie (1978) and Chambe & Hénoux (1979) gave explicit formulas of the energy deposit rate connected with the non-thermal ionization and excitation rate of the atoms. A series of computations including the non-thermal effects were carried out by Aboudarham (1986), Aboudarham & Hénoux (1986, 1987) and Hénoux & Aboudarham (1992) to explore white-light flare emission. Involved non-LTE calculations of the profiles of hydrogen, CaII K, NiI lines and the continuum emission in solar flares were also carried out (Fang et al. 1993; Hénoux, Fang & Gan 1993, 1995; Ding et al. 2002). The role of non-thermal electrons in the hydrogen and calcium lines of stellar flares was also explored by Ding & Fang (2000, 2001). Fang et al. (2002) reviewed the optical effects on solar chromosphere by non-thermal particles bombardment including non-thermal ionization and excitation, proton-hydrogen charge exchange and impact line polarization. Recently, Kašparová & Heinzel (2002) proposed a timesaving numerical method using "Multilevel Accelerate Lambda Iteration" to calculate the profiles of hydrogen Balmer lines including the partial-redistribution effects.

Diagnostics of the total energy flux of the non-thermal particle beam has been done in terms of "energy balance" (Aboudarham & Hénoux 1986, 1987), of "the head intensity slopes of Balmer and Paschen continua" (Zharkova & Kobylinsky 1993) and of "the intensity ratios of Hα/Hβ or Hα/Hγ at $\Delta\lambda = 0.4$ Å" (Kašparová & Heinzel 2002). In this paper, we propose to use the integrated intensity flux of the chromospheric lines for this purpose.

We briefly recall the methods of computing the non-thermal excitation and ionization of the atoms, etc., with solar temperature profiles taken from various semi-empirical models, the quiet-Sun VAL3C model (Vernazza et al. 1981), and the flare models F1 and F2 (Machado et al. 1980). A four-level plus continuum atomic model of hydrogen and a five-level plus continuum atomic model of ionized calcium are used. The non-thermal hydrogen ionization and excitation rates are taken from the series of papers of Fang et al. (1993), Hénoux et al. (1995), and included in the statistical equilibrium equations which are solved iteratively together with the equations of radiative transfer, hydrostatics equilibrium and particle conservation. A standard Lambda iteration is used and performed more than ten thousand times to achieve stable convergence; the final precision achieved is 10^{-5} in the radiative flux and 10^{-6} in the level population. Five broadening mechanisms - Doppler broadening, radiative damping, Van de Waals force, linear and quadratic Stark effect, are taken into account in the calculation of the line profiles. The partial frequency redistribution effect is considered for the Lyα line. Following Milkey & Mihalas (1973) and Vernazza et al. (1981), the angle-averaged redistribution function in isotropic radiation field can be written as:

$$R(\nu', \nu) = \gamma_s R^{II}(\nu', \nu) + (1 - \gamma_s)\phi_{\nu'}\phi_\nu, \tag{1}$$

where R^{II} is given by Kneer (1975), γ_s is the frequency-independent probability of coherent scattering and ϕ_ν represents the absorption profile normalized to $\int_0^\infty \phi_\nu d\nu = 1$. In our treatment, $\gamma_s = 0.95$ is adopted for the sake of simplicity.

Separate non-LTE calculations of hydrogen and ionized calcium profiles were carried out for three semi-empirical atmosphere models for four values of the total energy flux and three of the power index of electron and proton beams. It was supposed that the beams originate from the top of the coronal and inject vertically into the atmosphere. A fixed macroturbulence velocity field was used in our calculation.

In Section 2, we first relate the non-thermal excitation and ionization rate of hydrogen and ionized calcium to the energy deposit rate of particle beams. The influence of some key factors of the deposit rate on the intensity profiles are discussed in Section 3. Then we propose a way of using the contrast of the integrated intensity of hydrogen lines to estimate the total energy flux

of non-thermal particle beams and illustrate it by the major flare of 2002 July 23 in Section 4. Lastly, Section 5 summarises our conclusion and discussion on the diagnosis of the non-thermal particle beam bombardment.

2 ENERGY DEPOSIT RELATED TO NON-THERMAL EXCITATION AND IONIZATION RATE OF ATOMS

In a target atmosphere with ionization degree x, most of the energy of a particle beam deposit are due to collision with neutral hydrogen atoms and ambient free electrons and protons. Supposing the energy flux is proportional to $E^{-\delta}$, a given column density N can only be reached by a particle beam if its energy is greater than E_N given by Emslie (1978):

$$E_N = \Big[\Big(2+\frac{\bar{\beta}}{2}\Big)\frac{\bar{\gamma}KN}{\mu_0}\Big]^{\frac{1}{2}}, \tag{2}$$

where μ_0 is the cosine of the angle between the initial velocity vector and the solar vertical, $K = 2\pi e^4$, $\bar{\beta}$ and $\bar{\gamma}$ are the mean values along the particle trajectory of β and γ defined by Emslie (1978) and Chambe & Hénoux (1979), respectively. For a beam with a total energy flux at injection $\mathcal{F}_1$ above the lower energy cut-off E_1, the energy deposit rate at a column density N due to the non-thermal excitation and ionization of hydrogen, $dE^{\rm H}/dt$, is given by Emslie (1978) and Chambe & Hénoux (1979) as

$$\frac{dE^{\rm H}}{dt} = \frac{1}{2}(1-x)n_{\rm H}\Lambda'\frac{K\mathcal{F}_1}{{\rm E}_1^2}\Big(\frac{N}{N_1}\Big)^{\frac{-\delta}{2}}\int_0^{u_1}\frac{u^{\frac{\delta}{2}-1}}{(1-u)^{\frac{2+\bar{\beta}}{4+\beta}}}du, \tag{3}$$

where N_1 is the deepest column depth reached by the particles of energy E_1. $u = (\frac{E_N}{E})^2$, $u_1 = 1$ for $N > N_1$, and $u_1 = \frac{N}{N_1}$ for $N \le N_1$.

The rate of energy deposit described above is directly related to the non-thermal ionization rate (C_{1c}^B) of hydrogen and the non-thermal excitation rates (C_{1j}^B) of its various bound levels j ($j \neq 1$):

$$\frac{dE^{\rm H}}{dt} \simeq n_1\big(\sum_j \chi_{1j}C_{1j}^B + \chi_{1c}C_{1c}^B\big), \tag{4}$$

where n_1 is the population at the ground level of hydrogen atoms, χ_{1j} and χ_{1c} are the hydrogen excitation and ionization potential, respectively. Fang et al. (1993) and Hénoux et al. (1993) gave detailed expressions for C_{1c}^B and C_{1j}^B both for electron and proton beams:

$$C_{1c}^B = 1.73\times10^{10}\frac{1}{n_1}\frac{dE^{\rm H}}{dt}, \tag{5}$$

$$C_{12}^B = 2.94\times10^{10}\frac{1}{n_1}\frac{dE^{\rm H}}{dt}, \tag{6}$$

$$C_{13}^B = 5.35\times10^{9}\frac{1}{n_1}\frac{dE^{\rm H}}{dt}, \tag{7}$$

$$C_{14}^B = 1.91\times10^{9}\frac{1}{n_1}\frac{dE^{\rm H}}{dt}. \tag{8}$$

In the case of ionized calcium (C_{1j}^B(CaII) and C_{1c}^B(CaII)):

$$C_{14}^B({\rm CaII}) = 2.38\times10^{10}\frac{1}{n_1}\frac{dE^{\rm H}}{dt}, \tag{9}$$

$$C_{15}^{B}(\mathrm{CaII}) = 4.25 \times 10^{10} \frac{1}{n_1} \frac{dE^{\mathrm{H}}}{dt}, \tag{10}$$

$$C_{1c}^{B}(\mathrm{CaII}) = 4.69 \times 10^{10} \frac{1}{n_1} \frac{dE^{\mathrm{H}}}{dt}. \tag{11}$$

Equations (5) to (11) should be directly included in the statistical equilibrium, so the energy deposit rate dE/dt is essential and plays a crucial role in the calculation of the lines intensity: it enlightens us in our study of the non-thermal effect with respect to atmospheric models, particle nature, power index and total energy flux of particle beams.

3 EFFECTS OF THE NON-THERMAL PARTICLE BEAM BOMBARDMENT ON THE HYDROGEN AND CAII LINE PROFILES

3.1 Effects of the Total Energy Flux $\mathcal{F}_1$ and the Power Index δ

The total energy flux $\mathcal{F}_1$ and power index δ are two key parameters that describe non-thermal particle beams. Let us now consider the case of electron injection in three typical semi-empirical atmospheric models (VAL3C, F1 and F2). The non-thermal profiles of hydrogen (Fig. 1) and ionized calcium lines (Fig. 2) are plotted for four values of electron total energy flux (10^{12}, 5×10^{11}, 10^{11}, 10^{10} erg cm^{-2} s^{-1}) with power index $\delta = 4$. Given $T_e = T_i$, the highest value referenced in this paper, $\mathcal{F}_1 = 10^{12}$ erg cm^{-2} s^{-1}, may still be under the limit imposed by the return current stability.

In each panel of Figures 1 and 2, the thermal-dependent profile is also plotted for comparison. In general, the hydrogen and CaII lines appear in emission in the presence of a strong electron beam. The larger the total energy flux is, the stronger the line emission. As our results Figures 1 and 2 indicate, the hydrogen lines, especially the Lyman lines, react more strongly to the total energy flux than do the CaII K and CaII 8542 lines, but there are no such strong line-center enhancements in the Balmer lines as in Fang et al. (1993, fig. 1), and this is ascribed to insufficient iteration. An obvious central reversal appears in both the Balmer and Lyman lines and disappears gradually as the coronal mass and the temperature are increased. Consequently, the line-wings seem more sensitive to $\mathcal{F}_1$ than are the line-centers in each of the atmospheric models, particularly in the case of the Lyman lines. More explicitly, in the low-temperature, VAL3C model, the response of Hα line is mainly limited to the line-wings ($|\Delta\lambda| \gtrsim 0.5$ Å), while that of Lyα and Lyβ go further into the line-centers. However, in the flare model F1 the response of Balmer and Lyman lines to the total energy flux chiefly appears in their line-wings in various degrees, but for any line in the F2 model there is no marked enhancement because of the higher temperature and coronal mass.

It is important to understand the wavelength-dependent response from the point of view of the energy deposit rate (dE/dt) and the contribution function (CF), defined by Magain (1986),

$$\mathrm{CF} = S_{\mathrm{tot}} e^{-\tau} d\tau. \qquad (\mu_0 = 1) \tag{12}$$

All of the symbols have their usual meaning. The contribution function is wavelength-dependent and height-dependent, and describes the main formation region of the emission at a given wavelength; dE^{H}/dt represents the deposited energy distribution of non-thermal particle beams and is proportional to $\mathcal{F}_1$ as is shown in Eq. (3). The total energy flux $\mathcal{F}_1$, via the energy deposit, may modify to some extent the distribution of the main-formation-region of the emission at a given wavelength. The distribution of the CF at $\Delta\lambda = 0.3$ Å and 1.0 Å of Hα and Lyα lines (CF_0.3Å and CF_1.0 Å) are plotted separately for the thermal and non-thermal cases in Figure 3. Comparing the upper and lower panels of any line, one can find that the energy deposit rate affects not only the distribution of the contribution function but also its magnitude.

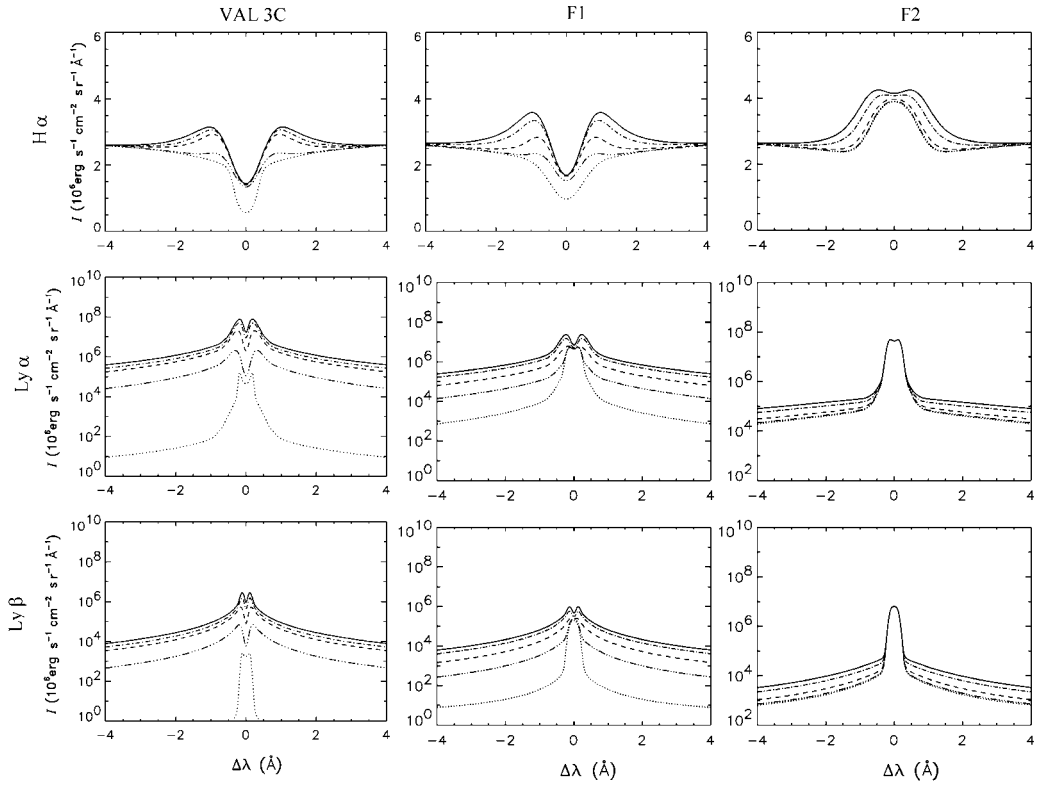

Fig. 1 Dependence of Hα, Lyα and Lyβ line profiles on the total energy flux for three semi-empirical atmospheric models — VAL3C (left), F1 (middle) and F2 (right), including the non-thermal effect for the electron beams with $\delta = 4$ and $\mathcal{F}_1 = 10^{12}$ (solid), 5×10^{11} (dash-dotted), 10^{11} (dash), 10^{10} (three-dots-per-dash) erg cm^{-2} s^{-1}, respectively. The thermal-dependent profile is also plotted in dotted lines. A Gaussian macroturbulence velocity of 20 km s^{-1} is adopted to convolve the line profiles in the flare atmospheric models F1 and F2.

On the other hand, the behaviors of the line profiles responding to various power indexes of the non-thermal particle beams are illustrated in Figure 4. From this figure, we can arrive at a similar conclusion to the total energy flux: the harder the energy spectrum is, the stronger the hydrogen line emission. However, the power index induces much less effect on the line intensity than does the total energy flux.

3.2 Electrons vs. Protons

Both electrons and protons may be accelerated and produce bombardment in the solar atmosphere during solar flares. On assuming they have the same total energy flux and power index, the non-thermal profiles of Hα and Lyα are compared in Figure 5. More information can be obtained from Lyα than from Hα, as mentioned above. For the Lyα line, the electron beam makes a clearer center reversal than does the proton beam, and this can be understood in terms of the energy deposit rate dE/dt. For the electron beam, there is an evident contrast between the initial and the peak value of dE/dt, not only in the magnitude but also in the depth in the

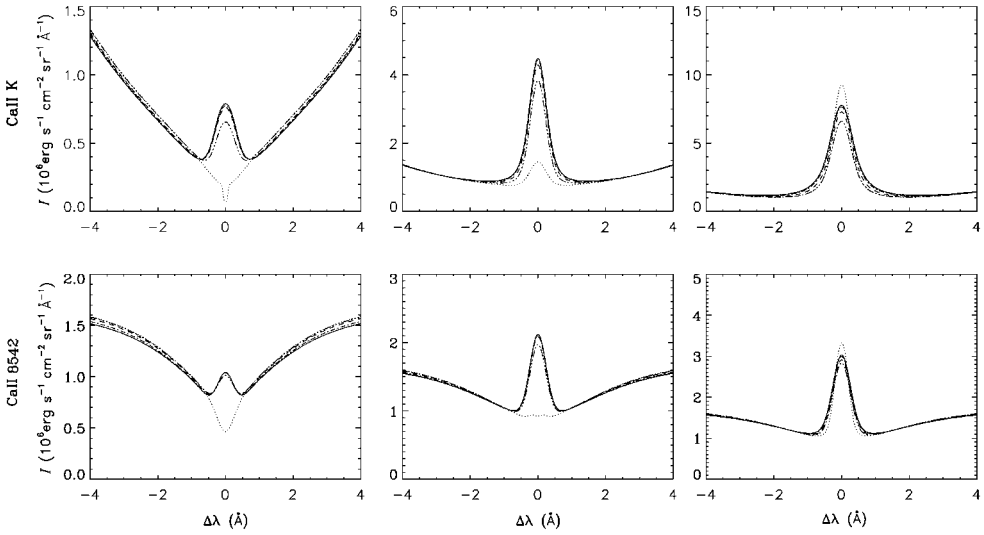

Fig. 2 Dependence of CaII K (upper) and CaII 8542 (lower) line profiles on the total energy flux for the semi-empirical atmospheric models— VAL3C (left), F1 (middle) and F2 (right). Different line styles have the same meaning as those in Fig. 1.

upper atmospheric layers (where the optically thick lines are mainly formed, e.g. the line centers of hydrogen lines), they go through before they begin to thermalize the ambient atmosphere in the deeper layers. For the proton beam, this contrast is not so evident. As a result, significant center reversal usually characterizes the electron beam bombardment, rather than the proton beam bombardment.

3.3 Effect of the Coronal Mass

In the foregoing sections, investigations were carried out for different atmosphere models with increasing temperature and coronal mass. Assuming the particle beam originates at the top of the corona, the coronal mass will inevitably consume some of the energy of the particles by collision. The results of calculations for the F1 model, ignoring the coronal mass, are shown in Figure 6 separately for the electron and proton beams. As we expected, the emission is strengthened for the hydrogen lines involved. This conclusion is consistent with the similar computations of Fang et al. (2002) and Hénoux et al. (1995) using other atmospheric models.

4 CONTRAST OF INTEGRATED INTENSITY

The dependence of the hydrogen line profiles on the non-thermal particle beam leads us to conclude that difference between the thermal and non-thermal intensity profiles is useful as a diagnostic of the total energy flux, rather than the power index of the particle beam during solar flares. Differing from Kašparová et al. (2002), we therefore suggest using the intensity integrated over the whole profile, i.e. the intensity flux, instead of the intensity at a certain wavelength. Here we adopt $|\Delta\lambda| \leq 4$ Å as the integration range. This is a reasonable choice because (1) in the Hα line the wavelengths $|\Delta\lambda| > 4$ Å are close to the continuum, which usually show little

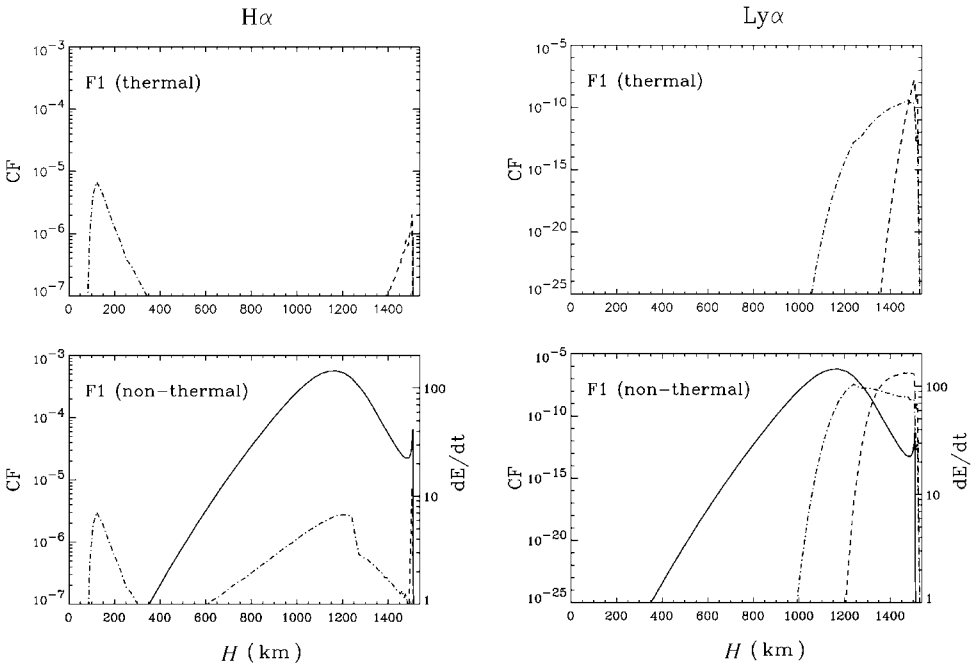

Fig. 3 Distribution of the contribution function of Hα (left) and Lyα (right) lines at $\Delta\lambda =$ 0.3 Å (dashed) and 1.0 Å (dash-dotted) in the thermal and non-thermal cases in the F1 flare model. The distribution of the energy deposit rate dE/dt (full line) is also plotted in the non-thermal case, assuming an electron beam wih $\delta = 4$ and $\mathcal{F}_1 = 10^{11}$erg cm^{-2}s^{-1}.

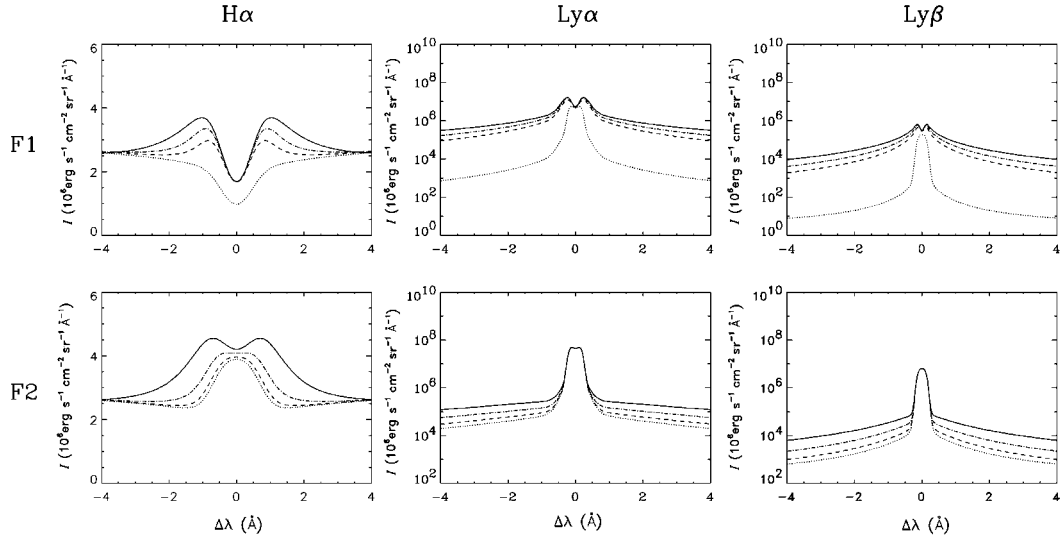

Fig. 4 Dependence of Hα (left), Lyα (middle) and Lyβ (right) line profiles on the power index for flare models F1 (upper) and F2 (lower), assuming the electron beam with $\mathcal{F}_1 = 5 \times 10^{11}$ erg cm^{-2} s^{-1} and δ=3 (solid), 4 (dash-dotted), 5 (dashed), respectively. The thermal profile is plotted in dotted lines and the same macroturbulence velocity is adopted as Fig. 1.

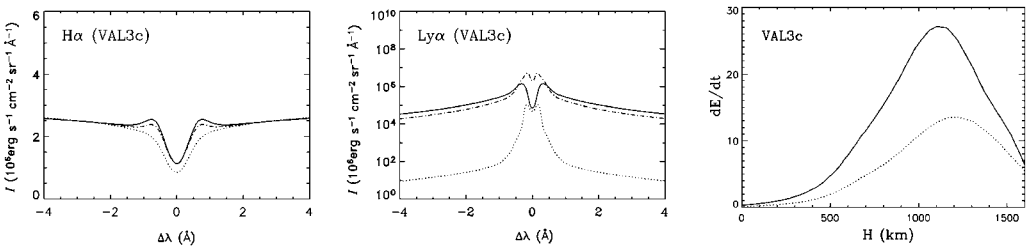

Fig. 5 Dependence of the Hα and Lyα line profiles on the nature of the particle beam (left and middle) and the energy deposit rate (right) in VAL3C model. In the first two panels, the non-thermal profile due to the electron (proton) beam is plotted in solid (dash-dotted) line, assuming the electron beam shares the same total energy flux ($\mathcal{F}_1 = 10^{10}$erg cm^{-2} s^{-1}) and the power index ($\delta = 3$) as the proton one. The thermal profile is plotted in dotted lines. In the right panel, dE/dt of this electron (proton) beam is plotted in solid (dotted) line.

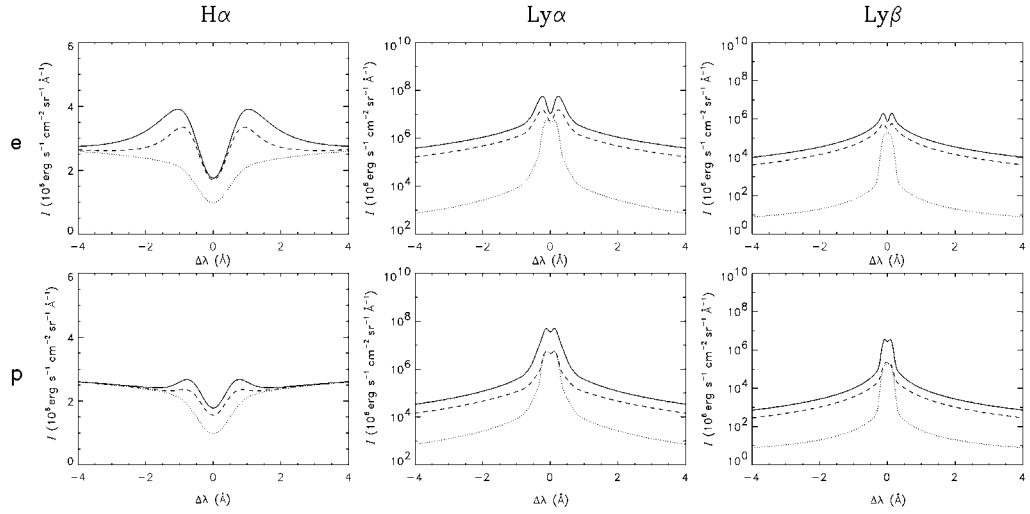

Fig. 6 Dependence of Hα (left), Lyα (middle) and Lyβ (right) line profiles on the coronal mass for the flare models F1, assuming an electron beam with $\delta = 4$ and $\mathcal{F}_1 = 5 \times 10^{11}$ erg cm^{-2} s^{-1} (upper) and a proton beam with $\delta = 4$ and $\mathcal{F}_1 = 1 \times 10^{11}$ erg cm^{-2}s^{-1} (lower). The case of ignoring the coronal mass ($m_0 = 0$) is plotted in solid line and the ordinary case ($m_0 = m_c$) is plotted in dashed line. The thermal profile is plotted in dotted lines and the same macroturbulence velocity is adopted as Fig. 1.

response to the non-thermal effect; (2) in the case of the Lyman lines, the intensities outside of this range can be ignored since it is typically two orders of magnitude lower than at the line centers. A parameter $(F - F_0)/F_0$ is introduced here to describe the contrast between the fluxes including the non-thermal effect (F) and excluding the non-thermal effect (F_0).

Figure 7 displays the dependence of the contrast of three hydrogen lines on the beam parameters in different atmospheric models. In each panel, the electron (proton) beam is marked by dotted (solid) lines, and in each set of dotted (solid) lines, the power index δ is equal to 3, 4 and 5 from top down. From this figure, one can see that the contrast monotonically increases with increasing total energy flux and decreasing power index. Furthermore, the total energy flux makes a greater difference than does the power index, especially in the cooler atmospheric models (e.g. VAL3C and F1). It is worth noting that the intensity flux of Lyα and Lyβ rises so much more rapidly and sharply with an increase in the total energy flux of electrons than with protons, that can be used to detect the bombardment by non-thermal electron beam during the impulsive phase of a flare. However, the Hα line is one of the conventional spectrum windows for flare observation. The 2002 July 23 2B/X4.8 flare serves as an example to interpret Figure 7. This flare is located at S13E72 on the solar disk and is associated with hard X-ray and radio emissions. Electron beam bombardment was a preferred candidate for explaining the broadened Hα line profile and the radial linear polarization during the impulsive phase (Firstova et al. 2003; Xu et al. 2003). A power index $\delta = 4 \sim 5$ is derived from the RHESSI and Nobeyama data. We take the theoretical VAL3C model for the pre-flare atmosphere and assume the temperature does not rise rapidly. Then the contrast between the observed and theoretical Hα flux is calculated to be about 0.128, see Figure 8. Given $\delta = 4$ we can estimate $\mathcal{F}_1$ to be about 1×10^{11} erg cm^{-2} s^{-1}. On the other hand, we use a semi-empirical chromospheric model (left panel of Fig. 9) to reproduce this profile (right panel of Fig. 9)(see Xu et al. 2003). By trial and error, an electron beam of $\mathcal{F}_1 = 10^{11}$ erg cm^{-2} s^{-1} and $\delta = 4$ is included in the calculation. Although the temperature structure of the semi-empirical model differs from that of VAL3C to some degree, we have obtained nearly consistent results regarding the total energy flux in a relatively time-saving way.

5 SUMMARY AND DISCUSSION

We present our calculations of Hα, Lyα, Lyβ, CaII K and CaII 8542 line profiles taking into consideration the non-thermal excitation and ionization due to the bombardment by a non-thermal particle beam for the quiet-Sun and two flare atmosphere models. Our investigation has led to the following conclusions:

(1) In general, bombardment of non-thermal particle beams during solar flares can be characterized by the intensity profiles of the hydrogen lines, which are greatly broadened, strengthened and central-reversed. In this process, electron beams are predominant particularly in the impulsive phase. In the case of CaII K and CaII 8542 lines, the emission is confined to the line-centers without causing any central reversal.
(2) The greater the total energy flux or the harder the energy spectrum, the stronger the line intensities. However, the intensity of the hydrogen lines, especially at the line-wings, are more sensitive to the total energy flux than to the power index.
(3) The response of the chromospheric lines to the non-thermal particle beam is weakened by the coronal mass.
(4) Bombardment by an electron beam is far more effective than bombardment by a proton beam of the same total energy flux.

In view of the above conclusions, we suggest that we use the contrast of the integrated intensity of the observed hydrogen line profiles to deduce the total energy flux of an electron beam. Although a major flare analysis has justified this diagnostics, there are still some controversial points. First, it is very important to estimate the thermal component of a profile, the atmospheric models used in our computations are semi-empirical models which cannot be generalized to the actual pre-impact atmospheric condition. For the impulsive phase, we would

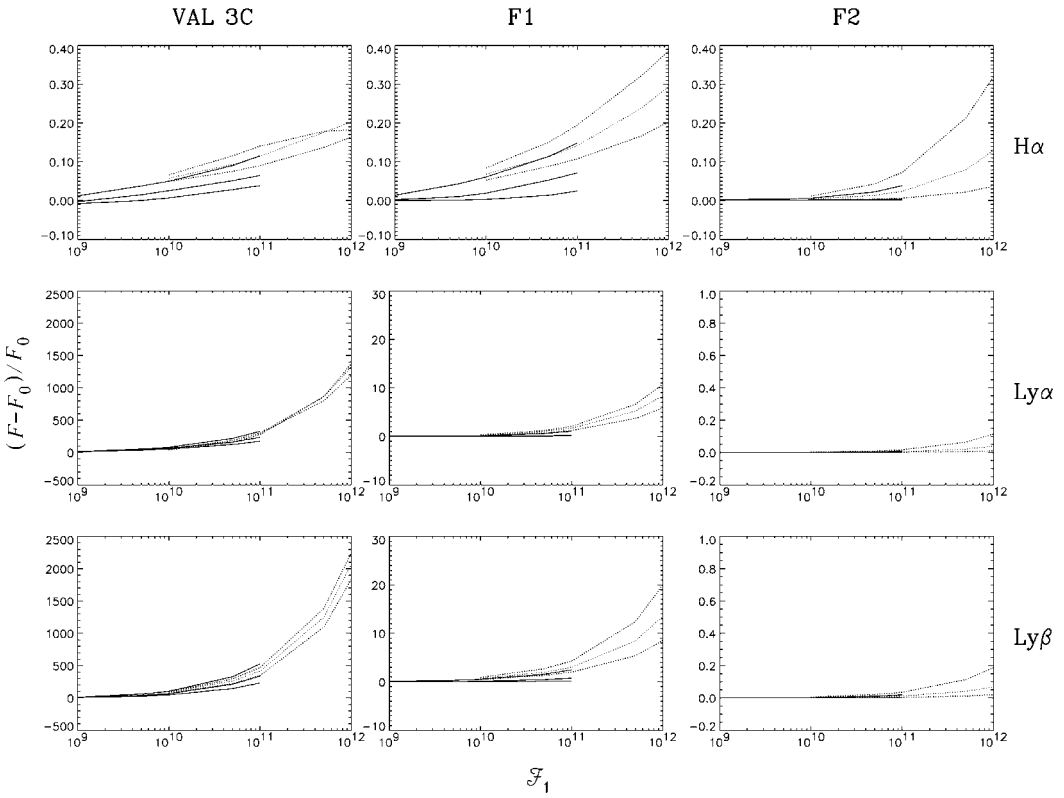

Fig. 7 Dependence of the contrast of the intensity flux on the parameters of the non-thermal particle beams. We take $\mathcal{F}_1$ from 1×10^{10} to 1×10^{12} erg cm^{-2} s^{-1} for the electron beam (dotted line), and $\mathcal{F}_1$ from 1×10^{9} to 1×10^{11} erg cm^{-2} s^{-1} for the proton one (solid line), with the power index $\delta = 3$, 4 and 5 from up to down respectively for each kind of particles.

suggest a co-spatial profile before a flare over a short time interval be used as the thermal component. It is possible that the atmospheric temperature and coronal mass do not rise rapidly at the impact of the non-thermal particles. However it is not the same case for the later phase or for long duration hard X-ray emission. The atmospheric condition is now changed and the profiles are now a mixture of thermal and non-thermal components, thus F_0 can only be estimated by a theoretical calculation, e.g. F1. Secondly, one can find a cross in the up left panel of Figure 7 between the electron beams of $\delta = 3$ and $\delta = 4$ when their total energy flux is large enough. It is due to the decrease of line wings intensity, which is induced by increased H^- density close to the temperature minimum region. Ding et al. (2003) indicated that in the early phase when the electron beam bombards an unheated atmosphere, the non-thermal ionization by the beam results in an increased H^- opacity which then reduces the continuum emergent intensity. Nevertheless, one can still use the curves in Figure 7 with a given power index δ obtained by other observations (e.g. hard X-ray or radio observation.) to deduce the total energy flux. Thirdly, following many previous authors, we take the low energy cut-off, E_1, of 20 keV for the non-thermal electron beam and 150 keV for the non-thermal proton beam. Although Gan et al. (2001a) have proposed a way to quantitatively measure the low energy cut-off based on

hard X-ray observations and although their statistical results (Gan et al. 2001b) showed that E_1 is likely to be $47 \sim 60$ keV, there is still no satisfactory conclusion on E_1. We will explore its influence on the line profiles in the future work.

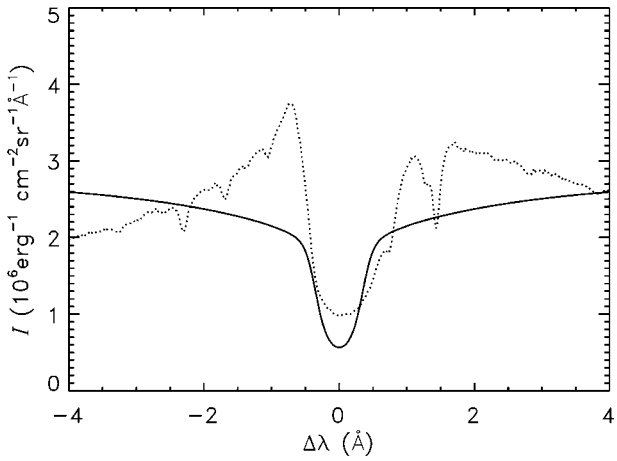

Fig. 8 One of the observed Hα line profiles at the impulsive phase of the flare on 2002 July 23 (dotted line), compared with the theoretical thermal profile of VAL3C model (solid line), which represents the condition of the target atmosphere before the flare. The intensity flux is obtained by integrating the intensity profiles over ± 4 Å.

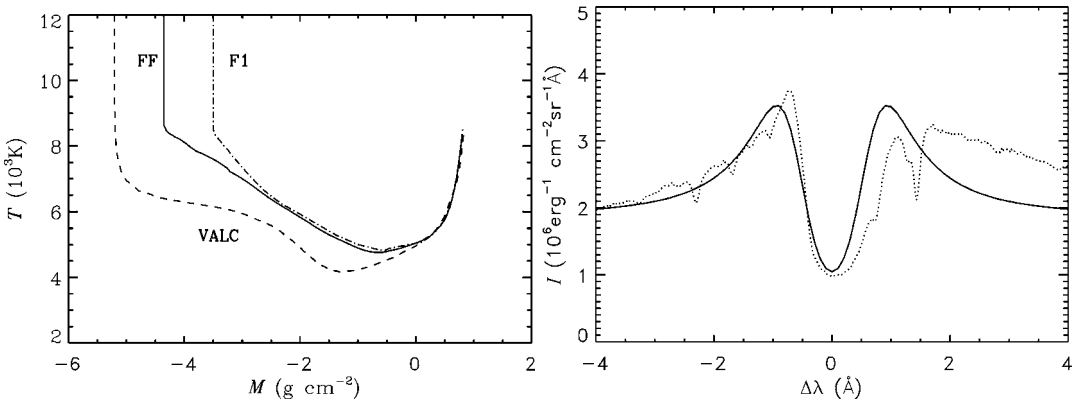

Fig. 9 Temperature distribution of the semi-empirical atmospheric model FF (left), which was used to compute the theoretical Hα line profile (right, the solid line) of the 2002 July 23 flare (see Xu et al. 2003). The computation was performed by assuming an electron beam of $\mathcal{F}_1 = 10^{11}$ erg cm^{-2} s^{-1} and $\delta = 4$ deduced from RHESSI data. The flare model F1 and the quiet-Sun model VAL3C are also shown for comparison. Dotted line in the right panel is the actually observed Hα line in the flare impulsive phase.

Acknowledgements We would like to express our gratitude to Prof. Ding M.D. for his advisable discussion. This work is supported by National Natural Science Foundation of China (Nos. 49990451, 1033040 and 10403003), and a key program from NKBRSF (G20000784).

References

Aboudarham J., 1986, Ph.D. Thesis, University of Paris VI
Aboudarham J., Hénoux J.C., 1986, A&A, 156, 73
Aboudarham J., Hénoux J.C., 1987, A&A, 174, 270
Chambe G., Hénoux J.C., 1979, A&A, 80, 123
Ding M. D., Liu Y., Yeh C.-T., et al., 2003, A&A, 403, 1151
Ding M. D., Qiu J., Wang H., 2002, ApJ, 576, 83
Ding M. D., Fang C., 2000, MNRAS., 317, 867
Ding M. D., Fang C., 2001, MNRAS., 326, 943
Emslie A. G., 1978, ApJ, 224, 241
Emslie A. G., Miller J.A., 2000, ApJ, 542, 513
Fang C., Hénoux J.C., Gan W.Q., 1993, A&A, 274, 917
Fang C., Ding M.D., Hénoux J.C., Gan W.Q., 2000, In: Proceeding of First Franco-Chinese Meeting on Solar Physics, ed. Fang C., Hénoux J. C., & Ding M. D., 147
Fang C., Xu Z., Ding M.D., 2002, Journal of The Korean Astronomical Socity, 35, 1
Firstova N. M., Xu Z., Fang C., 2003, ApJ, 595, L131
Gan W.Q., Li Y.P., Chang J., 2001a, ApJ, 552, 858
Gan W.Q., Li Y.P., Chang J., 2001b, ChJAA, 1, 453
Hénoux J. C., Aboudarham J., 1992, White-light Flares, In: Svestka Z., Jackson B.V., Machado M. E. eds., Proc. IAU Coll.133, Eruptive Solar Flares, Spring-Verlag, 118
Hénoux J. C., Fang C., Gan W. Q., 1993, A&A, 274, 923
Hénoux J. C., Fang C., Gan W. Q., 1995, A&A, 297, 574
Hudson H. S., 1972, SoPh, 24, 414
Kašparová J., Heinzel P., 2002, A&A, 382, 688
Kneer F., 1975, ApJ, 200, 367
Lin R.P., Hudson H.S., 1976, SoPh, 50, 153
Machado M.E., Avrett E.H., Vernazza J.E., et al.,1980, ApJ, 242, 336
Magain P., 1986, A&A, 163, 135
Milkey R. W., Mihalas D., 1973, ApJ, 185, 709
Miller J.A., Cargill, P.J., Emslie, A., et al., 1997, JGR., 102, 1463
Vogt E., Hénoux J. C., 1996, SoPh, 164, 345
Vogt E., Hénoux J. C., 1999, A&A, 349, 283
Vernazza J. E., Avrett E. H., Loeser R., 1981, ApJS, 45, 635
Xu Z., Firstova N. M., Chen Q. R., Fang C., 2003, ChJAA, 3, 266
Zharkova V. V., Kobylinsky V. A., 1993, SoPh, 143, 259